Interaction of solitary wave with a concentric structure with multiple porous outer walls

Zhenfeng Zhai [a], Weiwen Zhao [b], Decheng Wan [b,*], Dan Liu [a]

[a] School of Ocean Engineering and Technology, Sun Yat-Sen University, Zhuhai, 519000, China
[b] Computational Marine Hydrodynamics Lab (CMHL), School of Naval Architecture, Ocean and Civil Engineering, Shanghai Jiao Tong University, Shanghai, 200240, China

ARTICLE INFO

ABSTRACT

This paper gives an analytical solution for a plane solitary wave interaction with a concentric structure with coaxial multiple-layered porous walls. An analytical solution is obtained based on shallow water wave theory and eigenfunction expression matching. Furthermore, a series of simultaneous equations are used to determine potential coefficients. The accuracy of the present model is verified by comparing its output with published results. Meanwhile, the impact of various important parameters (i.e., the number of porous walls, annular spacing and porosity of walls) with respect to wave forces and relative wave height is examined. It is sufficient to safeguard the inner cylinder by using two-three porous walls. For multiple walls with different porous-effect parameters, the arrangement of the selected porous effect parameters has a marginal influence on the force of the impermeable cylinder. However, the minimum wave run-up on it can be observed when the coefficient of the porous walls increases from the outside to the inside. In addition, an impermeable cylinder with two concentric porous walls is investigated owing to its higher application prospects.

1. Introduction

Perforated breakwaters are typical marine structures. These are commonly used to reduce hydrodynamic loads on protected structures and safeguard coastal engineering structures that have significant environmental impacts and thereby, assure the stability of the port water surface for safely conducting docking and water operations. In practice, a coaxial cylindrical system with a porous exterior wall is applied extensively, e.g., the gravity offshore structure Ekofisk located in the North Sea, which can be considered as a porous concentric two-cylinder system (see Fig. 1). The gravity offshore structure was installed in 1973 at a water depth of around 75 m. It is 90 m high. The exterior and interior structure are 140 m and 89 m in diameter, respectively. For the concentric structure already in engineering application, a large number of theoretical, numerical and experimental studies have been carried out by researchers to further explore the rational and safe configuration for different sea conditions.

A model for explaining fluctuating flows in porous media that has been gaining attention since Sollitt and Cross (1973) is also the one that is most widely applied for porous structures. The porous wave-making theory was proposed by Chwang (1983). He discussed the importance of wave-effect parameters and porous-effect parameters. Wang and Ren (1994) derived the interaction between a sinusoidal wave and a concentric cylindrical system. Sankarbabu et al. (2007, 2008) discussed the diffraction problem of Airy waves and solitary waves interacting with a group of multiple dual-cylinder structures, respectively. By employing an experimental and numerical method, Vijayalakshmi et al. (2008) calculated the wave run-ups and wave forces on a concentric perforated structure. The scaled boundary finite element method has been used for the analytical solution of hydrodynamic forces on a concentric two-cylinder system (Song and Tao, 2007) and the numerical modeling of short-crested wave diffraction from a concentric three-cylinder system Tao et al. (2009). Zhu (2011) analysed the wave run-up around a coaxial porous system. The Mathieu function and modified Mathieu function were used by Wang et al. (2019) to calculate the analytical solution for the diffraction of short-crested waves around an elliptical cylinder using elliptical coordinates. Under the assumption of small-amplitude water wave motion and structural response, Zheng et al. (2020) investigated the hydroelastic interaction between water waves and a submerged porous elastic disc with negligible thickness in water of a finite depth. Sarkar and Bora (2021a, b) investigated the hydrodynamic performance of two modified compound cylindrical

---

* Corresponding author.
  E-mail address: dcwan@sjtu.edu.cn (D. Wan).

Fig. 1. Ekofisk gravity structure in the North Sea (Song and Tao, 2007).

structures: (1) a bottom-mounted surface-piercing partial-porous cylindrical compound structure, and (2) a concentric cylindrical system mounted on a cylindrical piece. Liang et al. (2021) investigated the scattering of water waves by impermeable and perforated horizontal plates considering both circular and elliptical plates, within the framework of linear potential flow theory. Mackay et al. (2021) investigated the wave-induced motions of floating cylinders with and without outer porous walls. It was found that the porous outer walls provide considerable damping and reduce motion response.

It is considered that the concentric two-cylinder system may be incapable of responding to a marine environment deteriorated by climate warming. More recently, Liu et al. (2018) employed a semi-analytical solution method to determine the water wave interaction with a concentric structure having multiple permeable external cylinders. It is well established that the near-shore sea area is a part of the shallow water area. When a wave propagates from a deep water area to an offshore area, with the increase in wave height, the water depth decreases, wave depth ratio increases, and non-linear effect becomes increasingly significant. This increases the error of the linear wave theory in the shallow water area. In actual coastal and marine engineering design of ports, it is more appropriate to use shallow water wave models to describe the interaction between waves and structures (Zhai et al., 2021). As a pioneer in the study of shallow water waves, Isaacson (1983) investigated the interaction of a solitary wave with a solid large cylinder by an approximate method by using linear boundary conditions. Weng et al. (2016) analysed the diffraction problem of cnoidal waves interacting with four porous cylinders. In recent years, many scholars have carried out studies on the interaction of solitary wave with many different types of structures using numerical modeling methods, e. g., a partially submerged thin porous wall(Miao and Wang, 2019), two series or parallel cylinders (Hafsia et al., 2021), combination of two thin concentric asymmetric porous arc walls(Zhai et al., 2022), a vertical cylinder at different locations on a slope beach(Kuai et al., 2021), two submerged rectangular obstacles(Ghafari et al., 2021), ect. In order to study the interaction between waves and structures more precisely and reliably, several scholars have conducted experimental studies. Yang et al. (2021) experimentally studied the combined flow-induced forces

between solitary wave-current and a vertical cylinder. Wang et al. (2021) completed an experiment on wave-induced run-up process and loads on cylinder in a solitary wave to simulate the nonlinear interaction between the tsunami-like wave and cylindrical structure.

To the authors' knowledge, there are no publications that report investigations on the interaction between solitary wave and a vertical cylinder with multiple concentric porous walls. However, this structure is being used in coastal engineering, e.g., a vertical breakwater with multiple porous walls constructed for the Dalian chemical production terminal, China Liu et al. (2018). Therefore, it is necessary to carry out theoretical research in this area to provide theoretical guidelines for subsequent engineering design.

In the present study, this work is to theoretically investigate the diffraction problem of solitary wave interaction with a concentric system having multiple concentric porous walls. By comparing the results of the present model with those of existing research, its accuracy is confirmed. We examined the effects of the number of porous walls, distance ratios, porous-effect parameters on the wave loads and run-ups on the present structure. Meanwhile, a concentric three-cylinder system was investigated as a particular case because of its larger application prospects in marine engineering. It should be noted that although the concentric three-cylinder system protects the interior structure better than the concentric two-cylinder system, it has some disadvantages, e.g., it needs higher engineering costs; the existence of the middle wall occupies the physical space, which may lead to the phenomenon of gap resonance during the transmission of the waves. With the current analysis method, concentric cylindrical systems can be assessed rapidly for hydrodynamic forces and wave run-ups. The paper is laid out as follows. The problem is formulated in Section 2. The validity of the proposed model is examined in Section 3. Then, the analytical results are presented in Section 4 before the work is summarised in Section 5.

2. Mathematical model

A schematic of a solitary wave interacting with an impermeable cylinder and multiple concentric porous walls having a negligible thickness is shown in Fig. 2. The still water depth is h. As shown in Fig. 2, we assumed that there are m ($m = 0, 1, ..., M$) concentric porous walls to protect the impermeable cylinder of radius R.

The $m - th$ wall radius is written in order from the inside to the outside as $R_m = R + m\Delta R$ (ΔR indicates the annular spacing between adjacent walls and between the first porous wall and impermeable cylinder). In this scenario, the fluid is divided into $M + 1$ subdomains: the domain Ω_1 ($R \leq r \leq R_1$), domains Ω_m ($R_{m-1} \leq r \leq R_m$, $2 \leq m \leq M$), and the outermost domain Ω_{M+1} ($r \geq R_M$). A cylindrical coordinate system $Or\theta z$, is applied for convenience. The z-axis is directed vertically upward from the bottom of the water. The fluid was assumed to be inviscid, incompressible, and with an irrotational motion. The velocity potential $\Phi(r, \theta, z, t) = \text{Re}[\varphi(r, \theta, z, t)]$. Here, φ is the complex velocity potential. Furthermore, φ in each region Ω_m ($m = 1, 2, ..., M + 1$) can be described as $\varphi^{(m)} = \varphi_I + \varphi_S^{(m)}$. Here, φ_I and $\varphi_S^{(m)}$ are the incident and scattered potential, respectively.

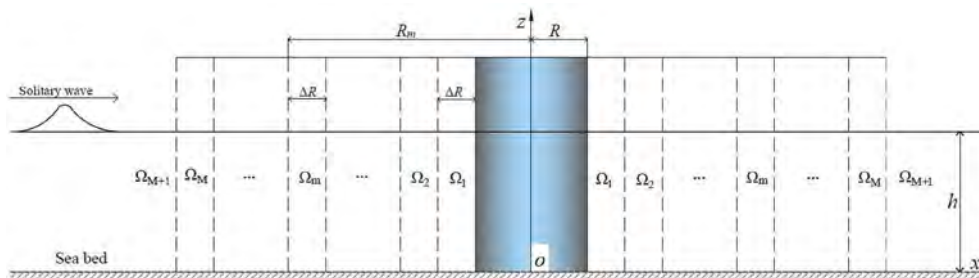The concentric structure is subjected to right-propagating solitary

Fig. 2. Definition sketch.

waves of height H and speed c_0 propagating to the positive direction of the $x-$ axis. When only first-order approximation is considered, the free-surface elevation η_I can be written in the following form according to Isaacson (1983):

$$\eta_1 = H \mathrm{sech}^2 \left[\sqrt{\frac{3H}{4d^3}} (x - ct) \right] \tag{1}$$

where H, t, $c = \sqrt{gh}$, and g are the wave height, time, wave speed for first-order approximation, and acceleration due to gravity, respectively. η_I can be represented by a Fourier integral as follows (Isaacson, 1983)

$$\eta_I = \frac{H}{2\pi} \int_{-\infty}^{+\infty} A(k) \cos k(x - ct) dk \tag{2}$$

where $i = \sqrt{-1}$, $A(k) = A(-k)$ and the Fourier transform $A(k)$ of η_I is

$$A(k) = \frac{4\pi h^3 k}{3H} \mathrm{cosech} \left[\pi k \sqrt{\frac{h^3}{3H}} \right] \tag{3}$$

Then, the corresponding incident potential φ_I can be expressed as follows:

$$\varphi_I = \frac{H}{2\pi\sqrt{h/g}} \int_{-\infty}^{+\infty} \frac{A(k)}{ik} e^{ik(x-ct)} dk = \frac{H}{\pi\sqrt{h/g}} \int_{0}^{+\infty} \frac{A(k)}{ik} e^{ikx} e^{-ikct} dk \tag{4}$$

Furthermore, φ_I can be rewritten as

$$\varphi_I = \int_{0}^{+\infty} \widehat{\varphi}_I [k(x - ct)] dk \tag{5}$$

where,

$$\widehat{\varphi}_I [k(x - ct)] = \frac{H}{\sqrt{h/g}} \frac{1}{\pi} \frac{A(k)}{ik} e^{ik(x-ct)} \tag{6}$$

Evidently, $\widehat{\varphi}_I[k(x-ct)]$ satisfies the relationship $\frac{\partial \widehat{\varphi}_I}{\partial x} - ik\widehat{\varphi}_I = 0$. Similarly, the scattered potential in the outermost region Ω_{M+1} can be written as $\varphi_S^{(M+1)} = \int_{0}^{+\infty} \widehat{\varphi}_S^{(M+1)} dk$. The integrated solution for scattering in the outermost region also satisfies this radiation condition. Furthermore, the radiation condition at infinity must be satisfied by $\widehat{\varphi}_S^{(M+1)}$, i.e.

$$\lim_{r \to \infty} \sqrt{r} \left(\frac{\partial \widehat{\varphi}_{\varphi_S}^{(M+1)}}{\partial r} - ik\widehat{\varphi}_{\varphi_S}^{(M+1)} \right) = 0 \tag{7}$$

Furthermore, Equation (4) can be expanded into a Fourier complex form using the following identity:

$$e^{ikx} = \sum_{n=0}^{\infty} \varepsilon_n J_n(kr) \cos(n\theta) \tag{8}$$

in which,

$$\varepsilon_n = \begin{cases} 1 & \text{for } n = 0 \\ 2i^n & \text{for } n \geq 1 \end{cases} \tag{9}$$

and $J_n(x)$ is the Bessel function of order n.

Thus, the incident wave potential in the outermost domain Ω_{M+1} can be written as

$$\varphi_I = \frac{H}{\sqrt{h/g}} \frac{1}{\pi} \int_{0}^{\infty} \frac{A(k)}{ik} e^{-ikct} \sum_{n=0}^{\infty} \left[\varepsilon_n J_n(kr) \cos(n\theta) \right] dk \tag{10}$$

The following matching conditions satisfied on the impermeable cylinder and the surfaces of these porous walls:

$$\frac{\partial \varphi^{(1)}}{\partial r} = 0 \ \text{for} \ r = R \tag{11}$$

$$\frac{\partial \varphi^{(m)}}{\partial r} = \frac{\partial \varphi^{(m+1)}}{\partial r} \ \text{for } r = R_m, \ m = 1, \ 2, ..., \ M \tag{12}$$

The boundary conditions on the porous walls can are given by (Williams et al., 2000)

$$\frac{\partial \varphi^{(m)}}{\partial r} = \frac{\partial \varphi^{(m+1)}}{\partial r} = \frac{G_m}{c} \left(\frac{\partial \varphi^{(m+1)}}{\partial t} - \frac{\partial \varphi^{(m)}}{\partial t} \right) \ \text{for } r = R_m, \ m = 1, \ 2, ..., \ M \tag{13}$$

where the porous-effect parameters G_m ($m = 1, \ 2, ..., \ M$) are denoted as $G_m = \rho c d_m / \mu$ (Chwang, 1983). Furthermore, ρ is the fluid density, μ is the viscosity constant, and d_m is the material constants having the dimension of length. In general, $G_m = 0$ represents an impermeable wall, and $G_m \to +\infty$ indicates that the wall vanishes. For typical offshore porous structures, the porous-effect coefficient G_m is normally less than 2. More detailed analysis on the determination of G_m value for porous structures can be found in Li et al. (2006). It is worth mentioning that the current model in this article has some limitations in calculating the wave loads acting on the impermeable cylinder, i.e., not predicting the pore pressure and soil stresses that result in an overestimation of the design of the porous structures.

3. Analytical derivation

The total velocity potential $\varphi^{(M+1)}$ in the outermost region, Ω_{M+1}, is composed of the incident potential φ_I and scatter potential $\varphi_S^{(M+1)}$. Where the scatter potential $\varphi_S^{(M+1)}$ must satisfy the radiation and boundary conditions in Equations (7), (12), and (13), respectively. It may be written in the following form:

$$\varphi_{ext}^{(M+1)} = \varphi_I + \varphi_S^{(M+1)} \tag{14}$$

The wave scattered potential for Ω_{M+1} can be written as

$$\varphi_S^{(M+1)} = -\frac{H}{\sqrt{h/g}} \frac{1}{\pi} \int_{0}^{\infty} \frac{A(k)}{ik} e^{-ikct} \sum_{n=0}^{\infty} \left[A_n^{(M+1)} H_n^{(1)}(kr) \cos(n\theta) \right] dk \tag{15}$$

where $A_n^{(M+1)}$ is the unknown complex potential coefficient and $H_n^{(1)}(x)$ denotes the Hankel function of the first type of order n. Thus, the total wave potential is given by

$$\varphi_{ext}^{(M+1)} = \frac{H}{\sqrt{h/g}} \frac{1}{\pi} \int_{0}^{\infty} \frac{A(k)}{ik} e^{-ikct} \sum_{n=0}^{\infty} \left[\varepsilon_n J_n(kr) + B_n^{(M+1)} H_n^{(1)}(kr) \cos(n\theta) \right] dk \tag{16}$$

The wave potential for the annual region Ω_m ($m = 2, 3, ..., M$) can be written as

$$\varphi^{(m)} = \frac{H}{\sqrt{h/g}} \frac{1}{\pi} \int_{0}^{\infty} \frac{A(k)}{ik} e^{-ikct} \sum_{n=0}^{\infty} \left[A_n^{(m)} J_n(kr) + B_n^{(m)} H_n^{(1)}(kr) \cos(n\theta) \right] dk \tag{17}$$

The wave potential for the interior region Ω_1 is given as

$$\varphi_{int}^{(1)} = \frac{H}{\sqrt{h/g}} \frac{1}{\pi} \int_{0}^{\infty} \frac{A(k)}{ik} e^{-ikct} \sum_{n=0}^{\infty} A_n^{(1)} U_n(kr) \cos(n\theta) dk \tag{18}$$

in which,

$$U_n(kr) = \begin{cases} J_n(kr) - \dfrac{J_n'(kR)}{H_n^{(1)'}(kR)} H_n^{(1)}(kr) & \text{for } R \neq 0 \\ J_n(kr) & \text{for } R = 0 \end{cases} \tag{19}$$

where $A_n^{(m)}$ ($m = 1, 2, ..., M$) and $B_n^{(m)}$ ($m = 2, 3, ..., M+1$) are potential coefficients to be determined.

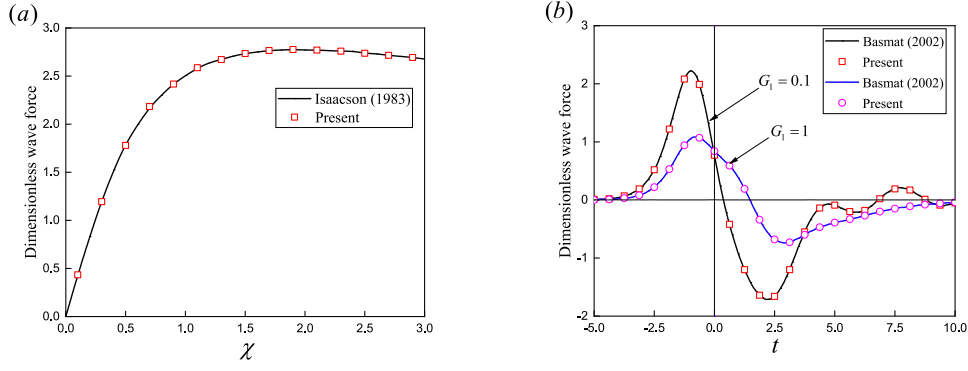Substitution of Equations 16–18 into Equations 12 and 13 yields.

Fig. 3. Comparison of the maximum dimensionless wave force on a solid cylinder between the present results and those of Isaacson (1983) and Basmat (2002), respectively:(a) plot of dimensionless wave force with wave parameter at $M = 0$; (b) plot of dimensionless wave force with corresponding time t at.$\chi = 1$, $R = 0$, $R_1 = 1$ m, $M = 1$
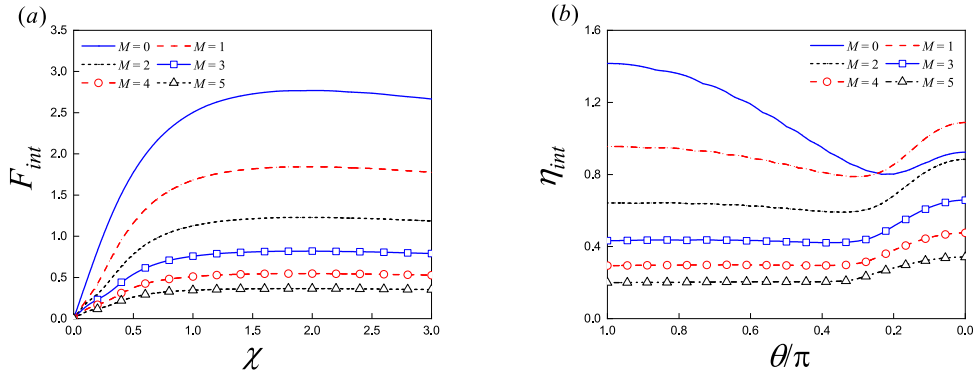

Fig. 4. Variations of the dimensionless wave force and run-up on the interior cylinder for various values of M:(a) wave force, $\Delta R/R = 1$, $G_m = 1$; (b) wave run-up, $\Delta R/R = 1$ $G_m = 1$, $\chi = 1.0$.
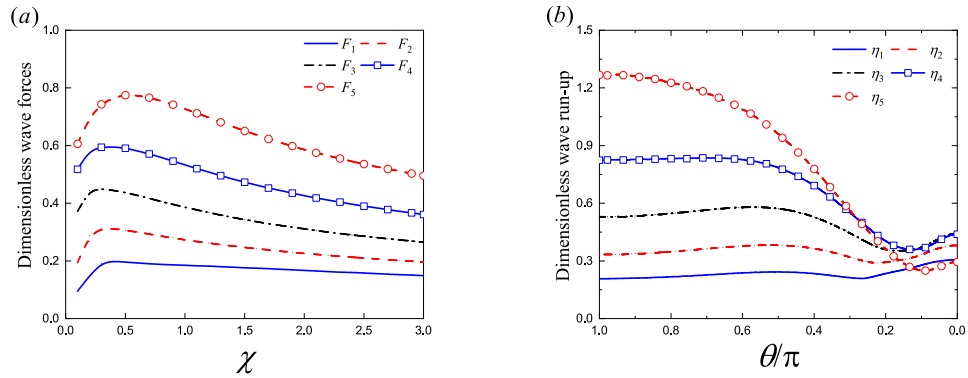

Fig. 5. Variations of the dimensionless wave force and run-up on the porous walls:(a) wave force $\Delta R/R = 1$, $G_m = 1$, $M = 5$; (b) wave run-up, $\Delta R/ R = 1$, $G_m = 1$, $M = 5$, $\chi = 1.0$.

For the M-th porous wall,

$$
\begin{cases}
B_n^{(M+1)}H_n^{(1)'}(kR_M) - A_n^{(M)}J_n^{'}(kR_M) - B_n^{(M)}H_n^{(1)'}(kR_M) = -\varepsilon_n J_n^{'}(kR_M) \\
B_n^{(M+1)}\left[H_n^{(1)'}(kR_M) - iG_M H_n^{(1)}(kR_M)\right] + iG_M A_n^{(M)}J_n(kR_M) + iG_M B_n^{(M)}H_n^{(1)}(kR_M) \\
= iG_M \varepsilon_n J_n(kR_M) - \varepsilon_n J_n^{'}(kR_M)
\end{cases}
$$

$$(20)$$

For the $m-$th $(m = 2, 3, ..., M-1)$ porous wall,

$$
\begin{cases}
A_n^{(m+1)}J_n^{'}(kR_{m-1}) + B_n^{(m+1)}H_n^{(1)'}(kR_{m-1}) - A_n^{(m)}J_n^{'}(kR_m) - B_n^{(m)}H_n^{(1)'}(kR_m) = 0 \\
A_n^{(m+1)}\left[J_n^{'}(kR_m) + iG_m J_n(kR_m)\right] + B_n^{(m+1)}\left[H_n^{(1)'}(kR_m) + iG_m H_n^{(1)}(kR_m)\right] \\
+ iG_m A_n^{(m)}J_n(kR_{m-1}) + iG_m B_n^{(m)}H_n^{(1)}(kR_m) = 0
\end{cases}
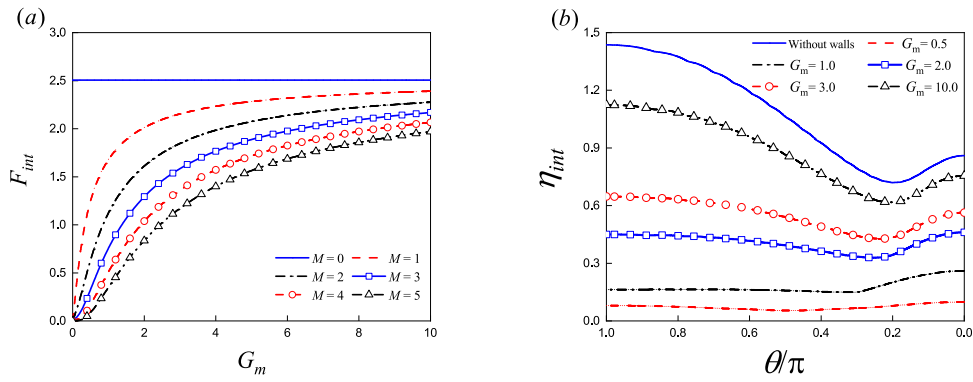$$

$$(21)$$

For the 1-st porous wall,

Fig. 6. Variations of the dimensionless wave force and run-up on the interior cylinder:(a) wave force, $\Delta R/R = 1$, $\chi = 1$; (b) wave run-up, $\Delta R/R = 1$, $\chi = 1.0$, $M = 5$.
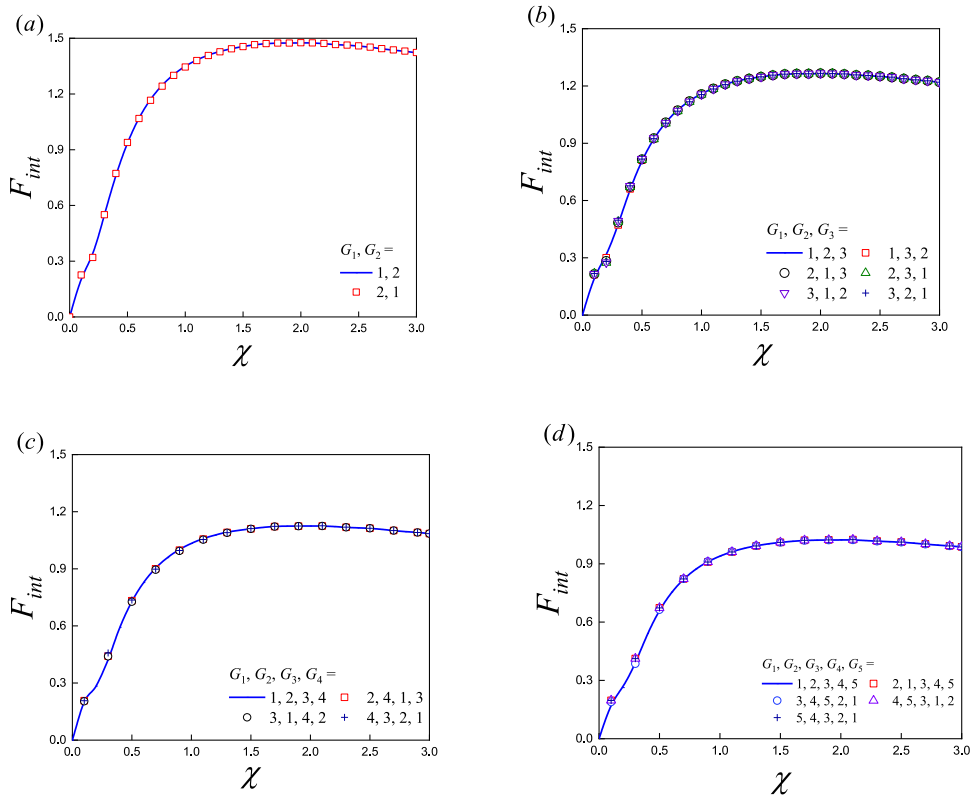

Fig. 7. Nondimensional wave forces on the solid interior cylinder with respect to χ for permutation and combination of porous-effect parameter G_m: (a) $M = 2$, (b) $M = 3$, (c) $M = 4$, and (d) $M = 5$.

$$\begin{cases} A_n^{(1)} U_n'(kR_1) - A_n^{(2)} J_n'(kR_1) - B_n^{(2)} H_n^{(1)'}(kR_1) = 0 \\ iG_1 A_n^{(1)} U_n(kR_1) + A_n^{(2)} \left[J_n'(kR_1) - iG_1 J_n(kR_1) \right] + B_n^{(2)} \left[H_n^{(1)'}(kR_1) - iG_1 H_n^{(1)}(kR_1) \right] = 0 \end{cases} \tag{22}$$

Equations $(20) - (25)$ constitute a complete set of equations with the unknown coefficients $A_n^{(1)}, A_n^{(2)}, \ldots, A_n^{(M)}, B_n^{(2)}, B_n^{(3)}, \ldots$, and $B_n^{(M+1)}$, for the entire fluid domain, which implies that these unknown coefficients can be obtained for the complete system of equations. By solving Equations $(20) - (22)$, the explicit expressions of these unknown coefficients are obtained in a form

$$A_n^{(1)} = \frac{\varepsilon_n P(M)}{A(M) \left[H_n^{(1)'}(kR_M) J_n'(kR_M) + P(M) \right] + B(M) \left[H_n^{(1)'}(kR_M) \right]^2} \tag{23}$$

$$B_n^{(M+1)} = \frac{\varepsilon_n \left\{ B(M) \left[H_n^{(1)'}(kR_M) J_n'(kR_M) + P(M) \right] + A(M) \left[J_n'(kR_M) \right]^2 \right\}}{A(M) \left[H_n^{(1)'}(kR_M) J_n'(kR_M) + P(M) \right] + B(M) \left[H_n^{(1)'}(kR_M) \right]^2} \tag{24}$$
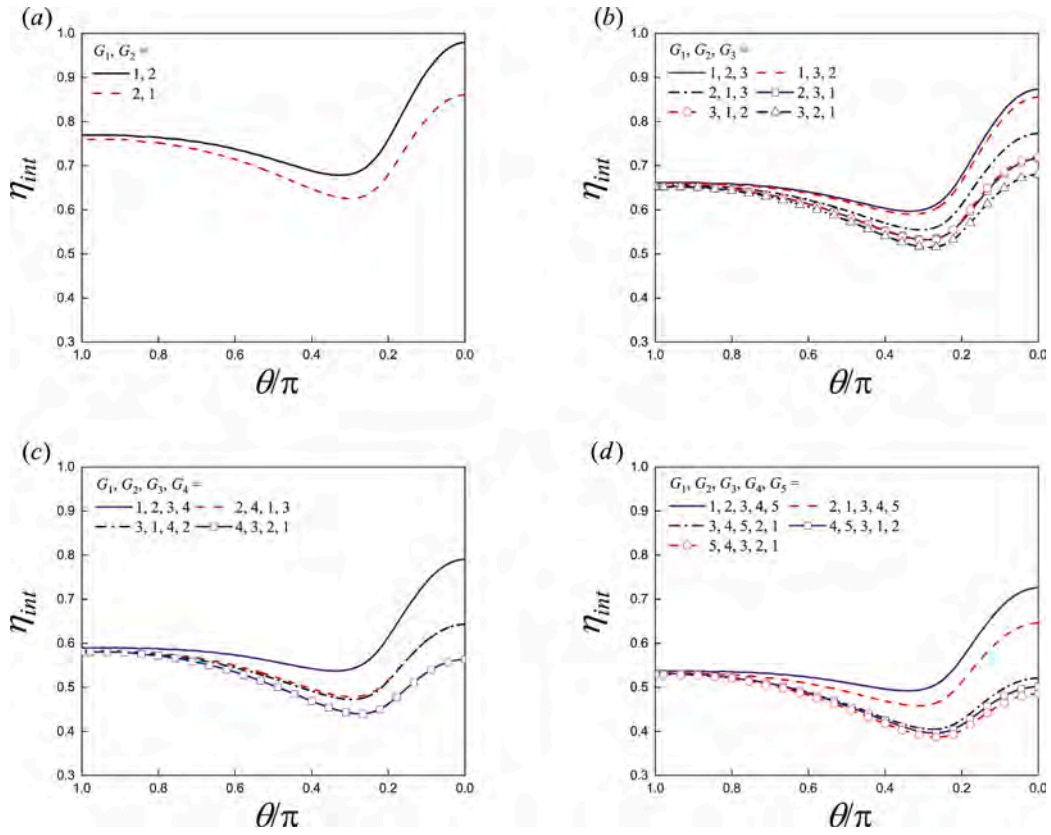
Fig. 8. Nondimensional wave forces on the solid interior cylinder for permutation and combination of porous-effect parameter G_m: (a) $M = 2$, (b) $M = 3$, (c) $M = 4$, (d) $M = 5$.
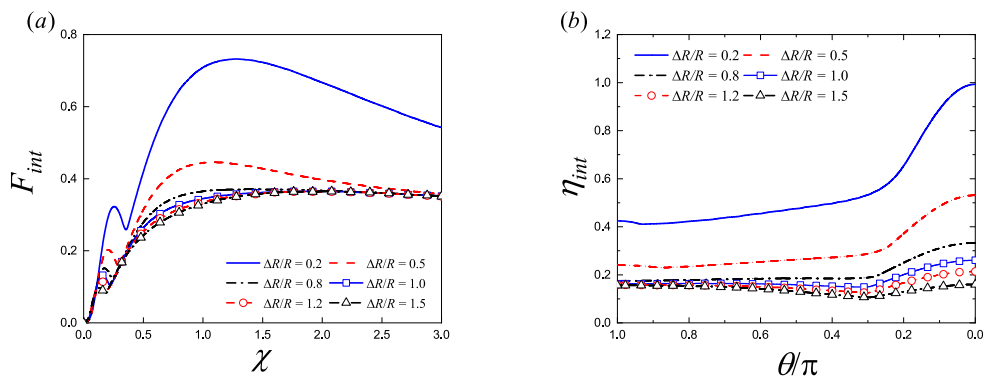

Fig. 9. Variations of the dimensionless wave force and wave runup on the interior cylinder for various values of $\Delta R/R$: (a) wave force, $Gm = 1$, $M = 5$; (b) wave run-up, $Gm = 1$, $M = 5$, $\chi = 1$.

$$
\begin{cases}
A_n^{(2)} = A_n^{(1)}\left\{ U_n'(kR_1)H_n^{(1)'}(kR_1) + iG_1\left[U_n'(kR_1)H_n^{(1)}(kR_1) - U_n(kR_1)H_n^{(1)'}(kR_1) \right] \right\}/P(1) = A_n^{(1)}A(2) \\
B_n^{(2)} = A_n^{(1)}\left\{ U_n'(kR_1)J_n'(kR_1) + iG_1\left[U_n'(kR_1)J_n(kR_1) - U_n(kR_1)J_n'(kR_1) \right] \right\}/Q(1) = A_n^{(1)}B(2) \\
A_n^{(3)} = A_n^{(1)}\left\{ A(2)\left[H_n^{(1)'}(kR_2)J_n'(kR_2) + P(2) \right] + B(2)\left[H_n^{(1)'}(kR_2) \right]^2 \right\}/P(2) = A_n^{(1)}A(3) \\
B_n^{(3)} = A_n^{(1)}\left\{ A(2)\left[J_n'(kR_2) \right]^2 + B(2)\left[J_n'(kR_2)H_n^{(1)'}(kR_2) + Q(2) \right] \right\}/Q(2) = A_n^{(1)}B(3) \\
\cdots \\
A_n^{(m)} = A_n^{(1)}\left\{ A(m-1)\left[H_n^{(1)'}(kR_{m-1})J_n'(kR_{m-1}) + P(m-1) \right] + B(m-1)\left[H_n^{(1)'}(kR_{m-1}) \right]^2 \right\}/P(m-1) \\
\quad = A_n^{(1)}A(m) \\
B_n^{(3)} = A_n^{(1)}\left\{ A(m-1)\left[J_n'(kR_{m-1}) \right]^2 + B(m-1)\left[J_n'(kR_{m-1})H_n^{(1)'}(kR_{m-1}) + Q(m-1) \right] \right\}/Q(m-1) \\
\quad = A_n^{(1)}B(m)
\end{cases}
\tag{25}
$$

where $A(2)$, $A(3)$, ..., $A(M)$, $B(2)$, $B(3)$, ..., and $B(M)$ are temporary variables. Furthermore,

$$
\begin{cases}
P(m) = iG_m\left[J_n'(kR_m)H_n^{(1)}(kR_m) - J_n(kR_m)H_n^{(1)'}(kR_m) \right] \\
Q(m) = iG_m\left[J_n(kR_m)H_n^{(1)'}(kR_m) - J_n'(kR_m)H_n^{(1)}(kR_m) \right]
\end{cases}
\tag{26}
$$

Based on this first-order approximation, the free-surface elevations in each region may be determined as follows:

$$
\eta_m = -\frac{1}{g}\frac{\partial \Phi_m}{\partial t} = \mathrm{Re}(\widehat{\eta}_m) \text{ for } z = h, \ m = 1, 2, ..., M+1
\tag{27}
$$

After obtaining the analytical solutions for the velocity potential in the different regions, we can calculate the linear wave loads by directly integrating the hydrodynamic pressure over the impermeable cylinder and porous walls. The pressure on the surface of the walls and the interior cylinder is written as

$$
P_m = -\rho\frac{\partial \Phi_m}{\partial t} = \mathrm{Re}(\widehat{P}_m) \text{ for } m = 1, 2, ..., M+1
\tag{28}
$$

The linear wave forces on the interior cylinder and porous walls along the incident wave direction are given by

In practice, for shallow water waves, a simple linear relationship between the overturning moment and wave loads exists (i.e., the overturning moment acting on the structure is exactly half of the corresponding force, indicating that they are experiencing similar changes). In addition, dimensionless factors $\rho g H R h$ and $\rho g H R_m h$ are employed to determine the dimensionless hydrodynamic loads, and the maximum dimensionless hydrodynamic loads F_{int} and F_m on the impermeable cylinder and porous walls are defined as follows:

$$
F_{\text{int}} = \frac{|F_{\text{int},x}|}{\rho g H R h}, \quad F_m = \frac{|F_{m,x}|}{\rho g H R_m h}
\tag{30}
$$

Similarly, the factor H was used to nondimensionalise the wave run-up, and the maximum dimensionless wave run-ups η_{int} and η_m on the impermeable cylinder and porous walls are defined as

$$
\eta_{\text{int}} = \frac{|\eta_{\text{int}}|}{H}, \quad \eta_m = \frac{|\eta_m|}{H}
\tag{31}
$$

4. Results and discussion

Based on the shallow water wave theory, the dimensionless wave parameter $\varsigma = H/k^2h^3 = 1/(k\sqrt{h^3/H})^2 = H/h \times 1/(kh)^2$ (H = wave

$$
\begin{cases}
F_x^M = -\int_0^h dz \int_0^{2\pi} [p_{M+1} - p_M]|_{r=R_M} R_M \cos\theta d\theta \\
\quad = -\rho g H R_M h \int_0^\infty A(k)e^{-ikct}\left[\varepsilon_n J_1(kR_M) + B_1^{(M+1)}H_1^{(1)}(kR_M) - A_1^{(M)}J_1(kR_M) - B_1^{(M)}H_1^{(1)}(kR_M) \right] dk \\
F_x^m = -\int_0^h dz \int_0^{2\pi} [p_{m+1} - p_m]|_{r=R_m} R_m \cos\theta d\theta \\
\quad = -\rho g H R_m h \int_0^\infty A(k)e^{-ikct}\left[\left(A_1^{(m+1)} - A_1^{(m)} \right)J_1(kR_m) + \left(B_1^{(m+1)} - B_1^{(m)} \right)H_1^{(1)}(kR_m) \right] dk \\
F_x^1 = -\int_0^h dz \int_0^{2\pi} [p_2 - p_1]|_{r=R_1} R_1 \cos\theta d\theta \\
\quad = -\rho g H R_1 h \int_0^\infty A(k)e^{-ikct}\left[A_1^{(2)}J_1(kR_1) + B_1^{(2)}H_1^{(1)}(kR_1) - A_1^{(1)}U_1(kR_1) \right] dk \\
F_{\text{int},x} = -\int_0^h dz \int_0^{2\pi} p_1|_{r=R} R \cos\theta d\theta \\
\quad = -\rho g H R h \int_0^\infty A(k)e^{-ikct}A_1^{(1)}U_1(kR)dk
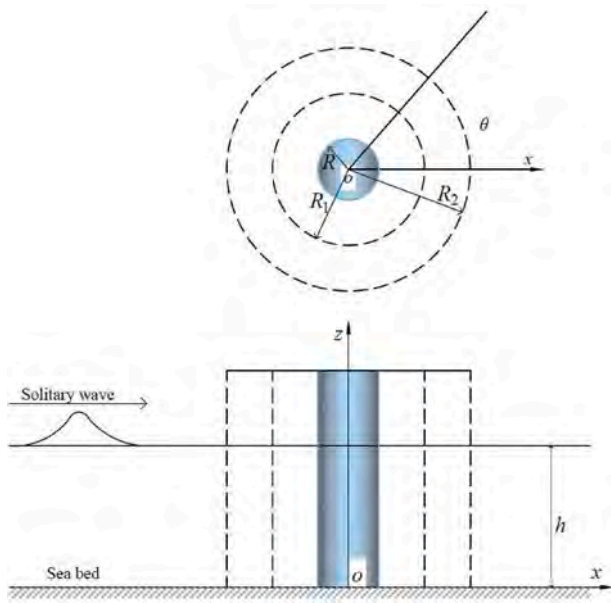\end{cases}
\tag{29}
$$

Fig. 10. Definition sketch for a vertical cylinder with two concentric porous walls.

height, k = wave number, and h = water depth) combines the effects of relative variations in wave height, wave number and water depth. $\sqrt{H/h^3}$ and k display a similar trend when ς is constant. Solitary wave is shallow water waves with infinitely long wavelengths. The wave number k is replaced by $\sqrt{H/h^3}$ in the actual calculation. $\sqrt{h^3/H}$ is the characteristic length of the solitary wave. As is established, the diffraction parameter ka represents the characteristic length of the wave and

the relative variation in water depth for the plane wave theory. Therefore, the corresponding diffraction parameter can be written as $\chi = \sqrt{H/h^3} \times R = \sqrt{HR^2/h^3}$ (R = the radius of the cylinder). As computational examples, the radius of the interior cylinder is $R = 10$ m, and the wave height is $H = 1$ m.

4.1. Model validation

Two classic solitary wave interactions with cylindrical structures can be used for testing the present theory: (1) When $M = 0$, the current structure transforms into an impermeable cylinder. The hydrodynamic loads on an impermeable cylinder obtained by the present study and the work of Isaacson (1983) are shown in Fig. 3a. The figure shows that the two results are consistent. (2) When $G_1 \neq 0$, $R_1 = 1$ m, $R = 0$, and $M = 1$, the current structure becomes a permeable cylinder. The wave forces on a permeable cylinder for the different wave-porous parameters obtained by the present study and the work of Basmat (2002) are shown in Fig. 3b. Note that the two results well agree. The above validation indicates that the proposed model is credible and can be used for further research.

4.2. Effect of the number walls M

Fig. 4 demonstrates the force and run-up on the interior cylinder for different numbers of porous walls M:(a) wave force, $\Delta R/R = 1$, $G_m = 1$; (b) wave run-up, $\Delta R/R = 1$ $G_m = 1$, $\chi = 1.0$. Note that the parameter $\Delta R/R = 1$ represents the ratio of the spacing between adjacent walls to the radius of the interior cylinder, and the ratio of the spacing of the first layer of wall to the interior cylinder to the radius of the interior cylinder are equal to 1, e.g., $R = 10$ m, $R1 = 20$ m, $R2 = 30$ m, $R3 = 40$ m, $R4 = 50$ m, $R5 = 60$ m for $M = 5$, so the $\Delta R = 10$ m; $G_m = 1$ represents the permeability coefficient of each permeable wall layer is equal to 1, e.g.,
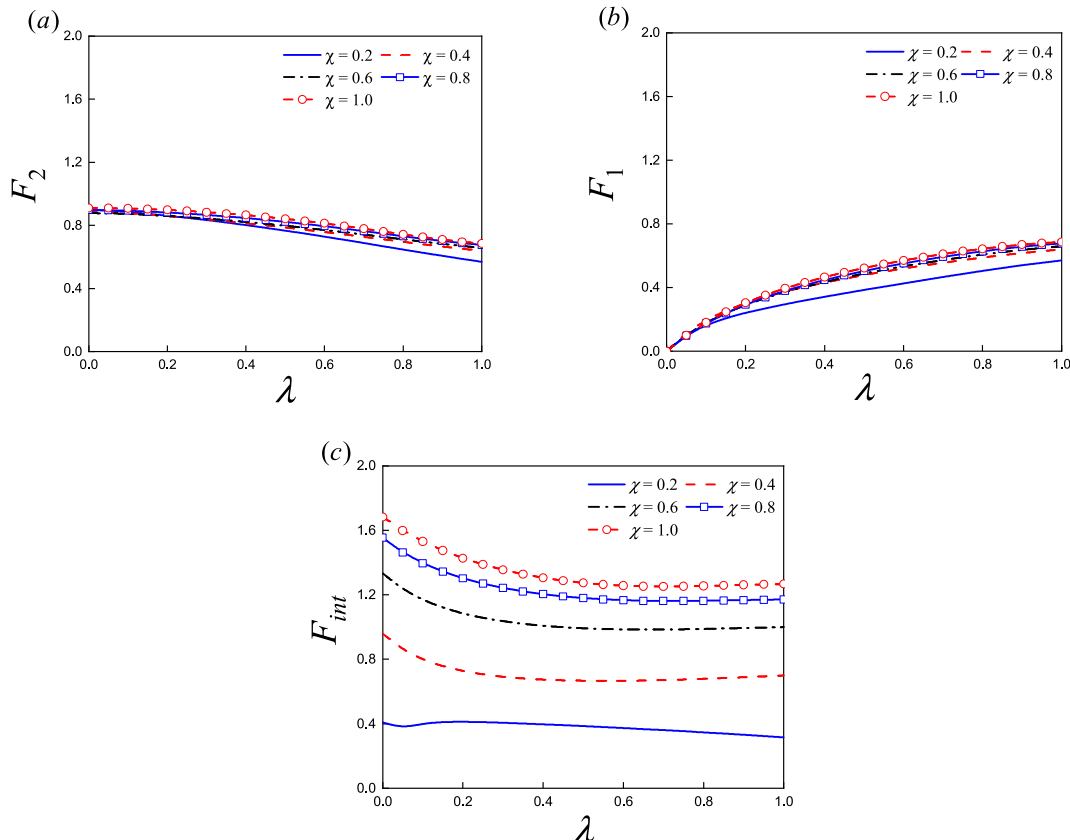

Fig. 11. Nondimensional wave forces on the structure with respect to the ratio λ for different values of χ: (a) F_2, (b) F_1, (c) F_{int}.
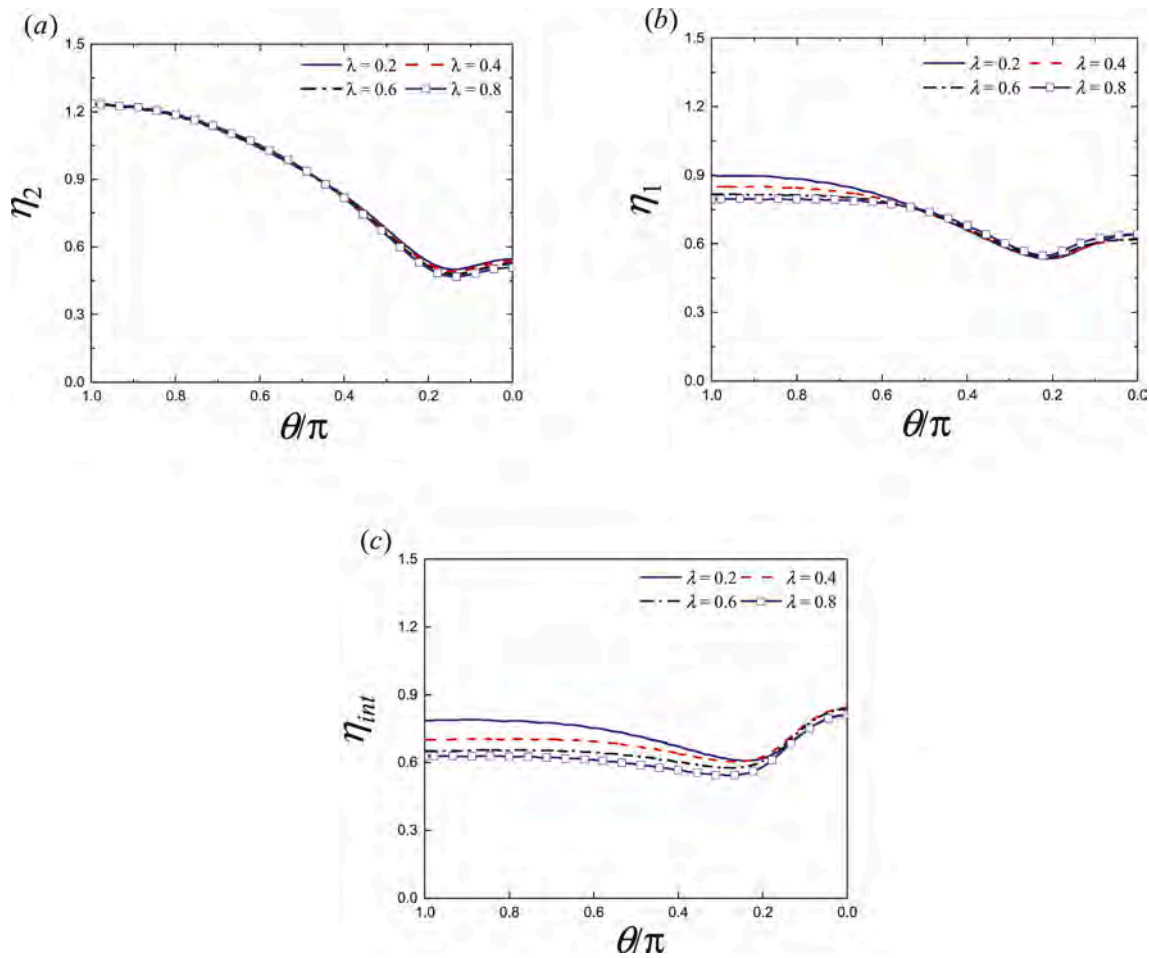
Fig. 12. Nondimensional wave run-up on the structure with respect to the ratio λ for different values of χ: (a) η_2, (b) η_1, (c) η_{int}.

G1 = G2 = G3 = G4 = G5 = 1 for M = 5. As shown in Fig. 4a, the wave forces on the interior cylinder exhibit a similar trend for various values of M, i.e., first increase monotonically, attain their peak values at approximately χ = 1, and then keep remain constant. As anticipated, the forces acting on the interior cylinder decrease gradually as M increases. The peak value of the wave force attains 2.77, 1.84, 1.23, 0.82, 0.55, and 0.37 for M of 0 − 5, respectively. Compared with that for the peak value of wave force on the isolated cylinder (M = 0), the reduction is approximately 34%, 56%, 70%, 80%, and 87% in the amplitude of the wave force for M of 1–5, respectively, which implies that the interior cylinder obtains sufficient protection when M = 2 or 3. However, $M = 3$ may be the best option considering the construction cost. As shown in Fig. 4b, on the windward side, the wave run-up decreases gradually as M increases. Meanwhile, on the leeward side, the wave run-up decreases mildly except for $M = 1$. It should be noted that $\theta/\pi = 0$ represents the leeward side of the structure, and $\theta/\pi = 1$ represents the windward side of the structure. $\theta/\pi = 1 \rightarrow 0$ means the intersection of the structure with the negative $x-$ axis is rotated counterclockwise to the positive $x-$ axis. When $M \geq 2$, the wave run-ups display a similar trend, i.e., the wave run-up decline marginally for $0 \leq \theta/\pi \leq 0.3$ and remain steady for $0.3 \leq \theta/\pi \leq 1$. When $M = 1$, on the leeward side, the wave run-up on the interior cylinder is higher than the isolated cylinder ($M = 0$). This is because of the reflection of waves by the porous exterior wall.

Fig. 5 demonstrates the forces and run-up on the porous walls:(a) wave force $\Delta R/R = 1$, $G_m = 1$, $M = 5$; (b) wave run-up, $\Delta R/R = 1$, $G_m = 1$, $M = 5$, χ = 1.0. As shown in Fig. 5a, the wave forces acting on the five porous walls exhibit a similar trend, i.e., a dramatic increase at smaller values of χ until it approaches a maximum value in the neighbourhood of χ = 0.4, followed by a monotonous decrease towards its

asymptotic values. Owing to the protective effect of the exterior porous wall on the interior structure including the interior porous walls and impermeable cylinder, the closer the porous wall is to the impermeable interior cylinder, the lower is the wave load that it is subjected to. As shown in Fig. 5b, on the windward side, the wave run-up decreases gradually as the porous wall approaches the interior cylinder. However, on the windward side, due to the complex reflection of waves between the porous walls, the change rule of wave run-up is not obvious.

4.3. Effect of porous parameter

In this section, the real physical meaning of the porous-effect parameter is visually described to improve reader understanding. The porous-effect parameter is related to the density and radii of thin-walled holes, indicating that more densely packed holes and larger hole radii increase the radial flow velocity when the wave passes through the porous region of a structure. Fig. 6 demonstrates the force and run-up on the interior cylinder:(a) wave force, $\Delta R/R = 1$, χ = 1; (b) wave run-up, $\Delta R/R = 1$, χ = 1.0, M = 5. Equation (13) shows that both sides of the wall have equal radial velocity and that the difference in pressure between these is proportional. It is important to note that G_m is related to the density and radii of the thin-walled holes. This implies that for a larger G_m, more densely packed holes and larger hole radii cause a higher radial flow velocity when the wave passes through the porous region of the structure. A bigger G_m implies that more waves can pass through the porous structure. Evidently, the wave force acting on the interior cylinder decreases gradually as M increases. From Fig. 6a, the wave force on the interior impermeable cylinder increases monotonically towards its asymptotic value ($M = 0$) as G_m increases, and the
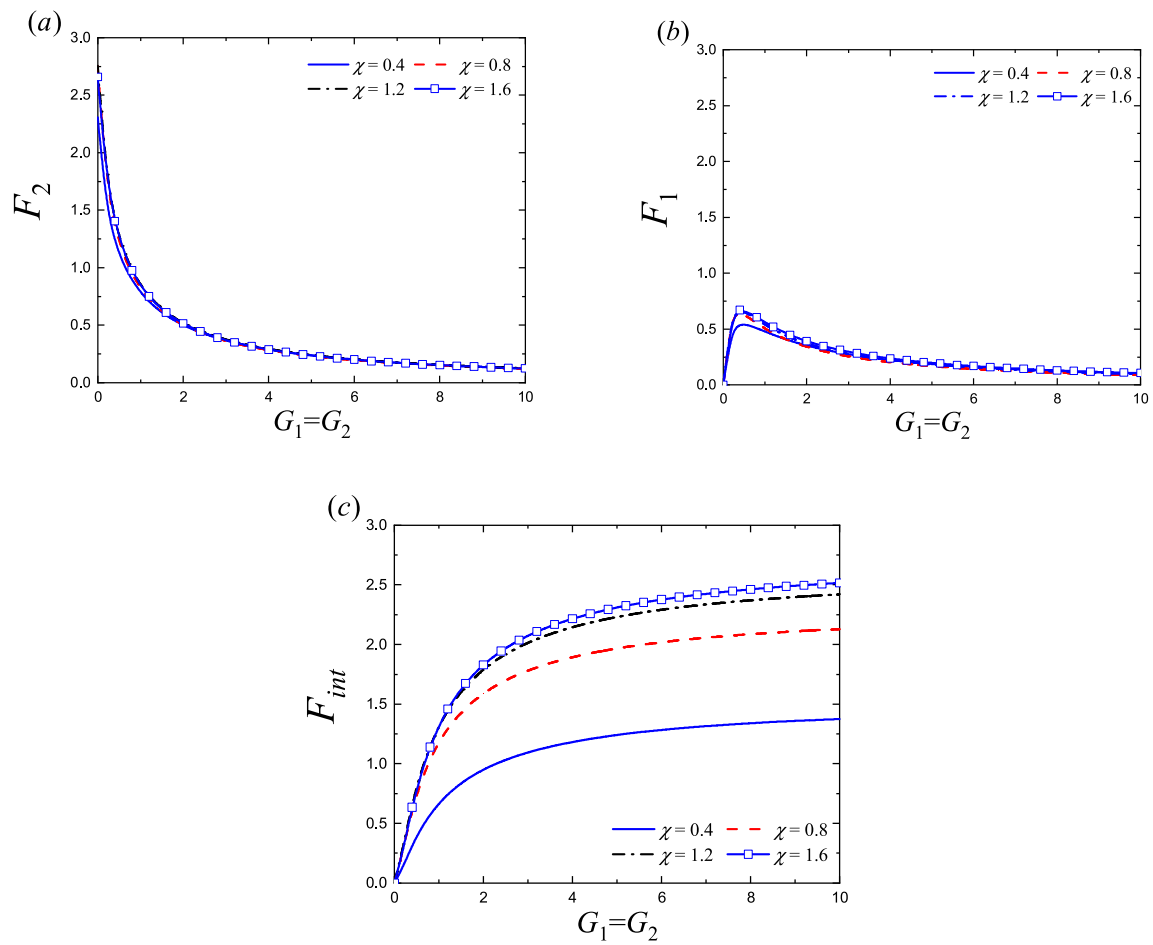
Fig. 13. Nondimensional wave forces on the structure with respect to the ratio G_m for different values of χ: (a) F_2, (b) F_1, (c) F_{int}.
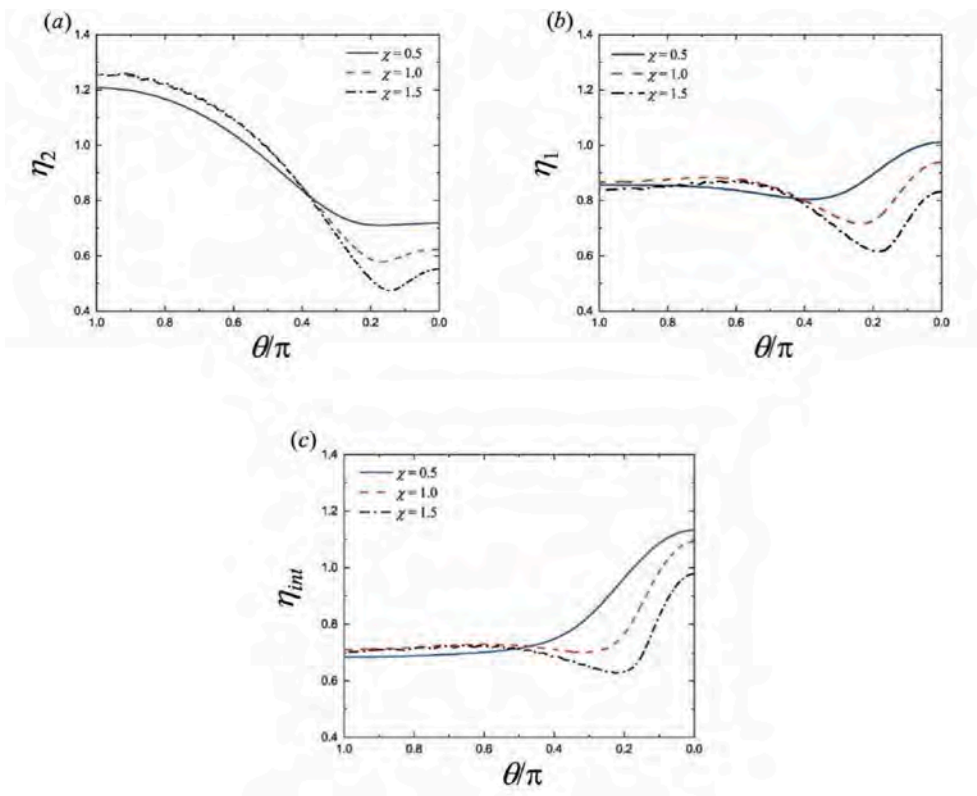

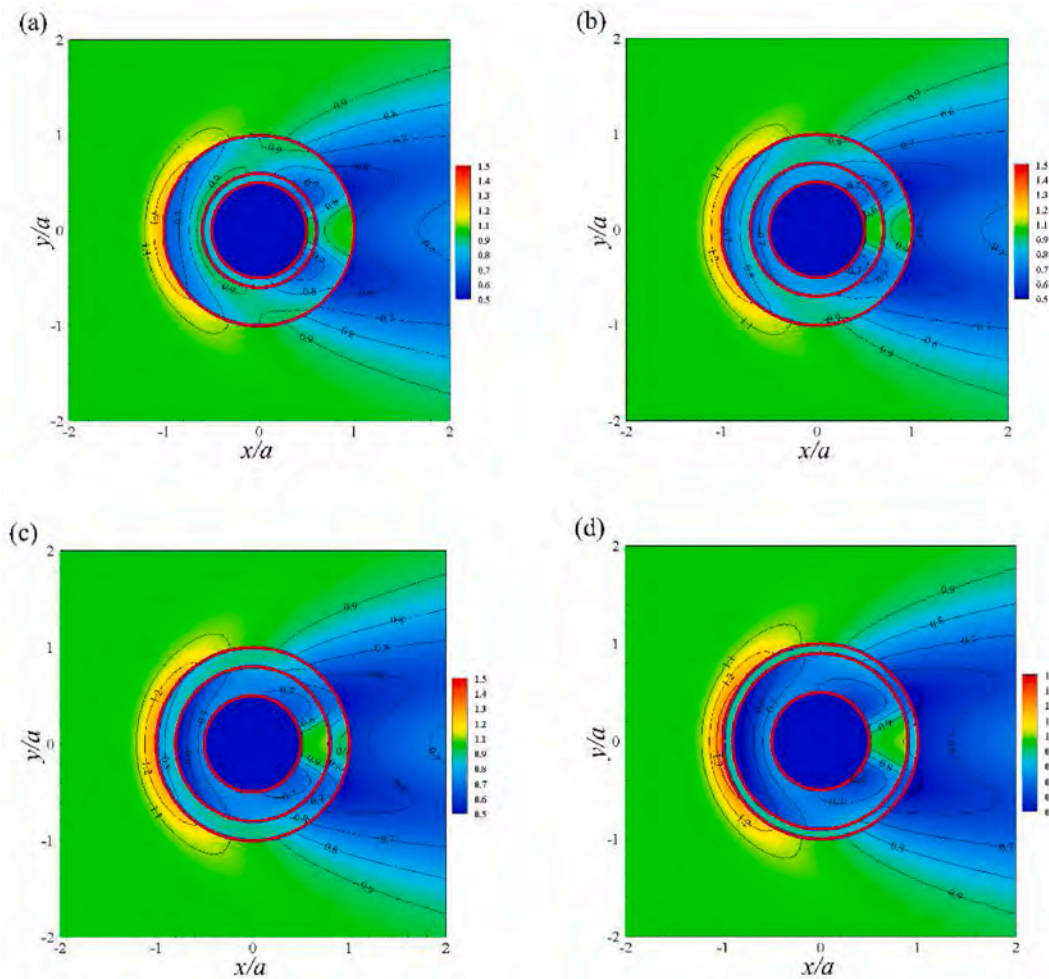**Fig. 14.** Nondimensional wave run-up on the structure for different values of χ: (a) η_2, (b) η_1, (c) η_{int}.

Fig. 15. The relative wave height in the vicinity of a concentric structure for different values of λ: (a) λ = 0.2, (b) λ = 0.4, (c) λ = 0.6, (d) λ = 0.8.

rate of convergence to an asymptotic value becomes more gradual as M increases. As indicated in Fig. 6b, on the windward and leeward sides, the wave run-up increases monotonously as G_m increases, which is owing to the reduced wave protection provided by the permeable walls. Moreover, the difference in the amplitude of wave run-up on the windward and leeward sides of the interior cylinder increases as G_m increases, and the wave run-up around the interior cylinder become closer and closer to the isolated cylinder.

Fig. 7 demonstrates the forces F_{int} caused by a solitary wave on the impermeable cylinder with respect to χ when $\Delta R/R = 1$. As shown in Fig. 7a − 7d, for the different values of M, the permutations of the selected porous-effect parameters have negligible effect on the wave force. For example, there are six combinations for $M = 3$ when each wall has a different porous parameter: $G_1 = 1, G_2 = 2, G_3 = 3$; $G_1 = 1, G_2 = 3$, $G_3 = 2$; $G_1 = 2, G_2 = 1, G_3 = 3$; $G_1 = 2, G_2 = 3, G_3 = 1$; $G_1 = 3, G_2 = 2, G_3 = 1$; and $G_1 = 3, G_2 = 1, G_3 = 2$. It is noteworthy that the force almost equal for the six cases. Similarly, there are 24 and 120 combinations of porous-effect parameters for $M = 4$ and 5, respectively, and the force is also maintained constant (for convenience, only a few of the results are shown in Fig. 7c and d. This may indicate that the arrangement of the porous-effect parameter has no effect on the safety of the interior structure. Mathematically, the permutation of the permeability coefficients does not affect the value of the unknown coefficient $A_n^{(1)}$ and therefore it does not change the wave load acting on the interior cylinder.

Fig. 8 demonstrates the maximum dimensionless wave run-up η_{int} around the impermeable interior cylinder for permutation and combination of G_m when $\Delta R/R = 1$ and $\chi = 0.8$. As is evident from Fig. 8(a) − 8(d), on the windward side, the permutation and combination of G_m has negligible effect on the wave run-up around the interior cylinder. The peak value of the wave run-up is observed when the coefficient of the porous walls increases from the outside to the inside. Conversely, the trough values of the wave run-up can be observed as the coefficient of the porous walls decreases. Figs. 7 and 8 together indicate that porous walls wherein the coefficient of porosity decreases from the outside to the inside may be highly effective for concentric structures with multiple walls.

4.4. Effect of annual spacing

Fig. 9 demonstrates the force and wave runup on the interior cylinder for various values of $\Delta R/R$: (a) wave force, $Gm = 1, M = 5$; (b) wave run-up, $Gm = 1, M = 5, \chi = 1$. From Fig. 9a, the forces on the cylinder decrease monotonically as $\Delta R/R$ increases, and the amplitude of the reduction in wave force becomes negligible with a further increase in $\Delta R/R$. Therefore, when $\Delta R/R > 0.8$, the reduction of the force on the impermeable cylinder by increasing the annular spacing further a high-cost-low-benefit option in engineering. As shown in Fig. 9b, the change rule of wave run-up on the interior cylinder is very similar to the wave force as $\Delta R/R$ increases. Moreover, when $\Delta R/R > 0.8$, the amplitude of the wave run-up on the interior cylinder no longer varies significantly. Overall, the better $\Delta R/R$ value is around 0.8. Thus, the Value of $\Delta R/R$ is set to 1 for the convenience of calculation in this article.
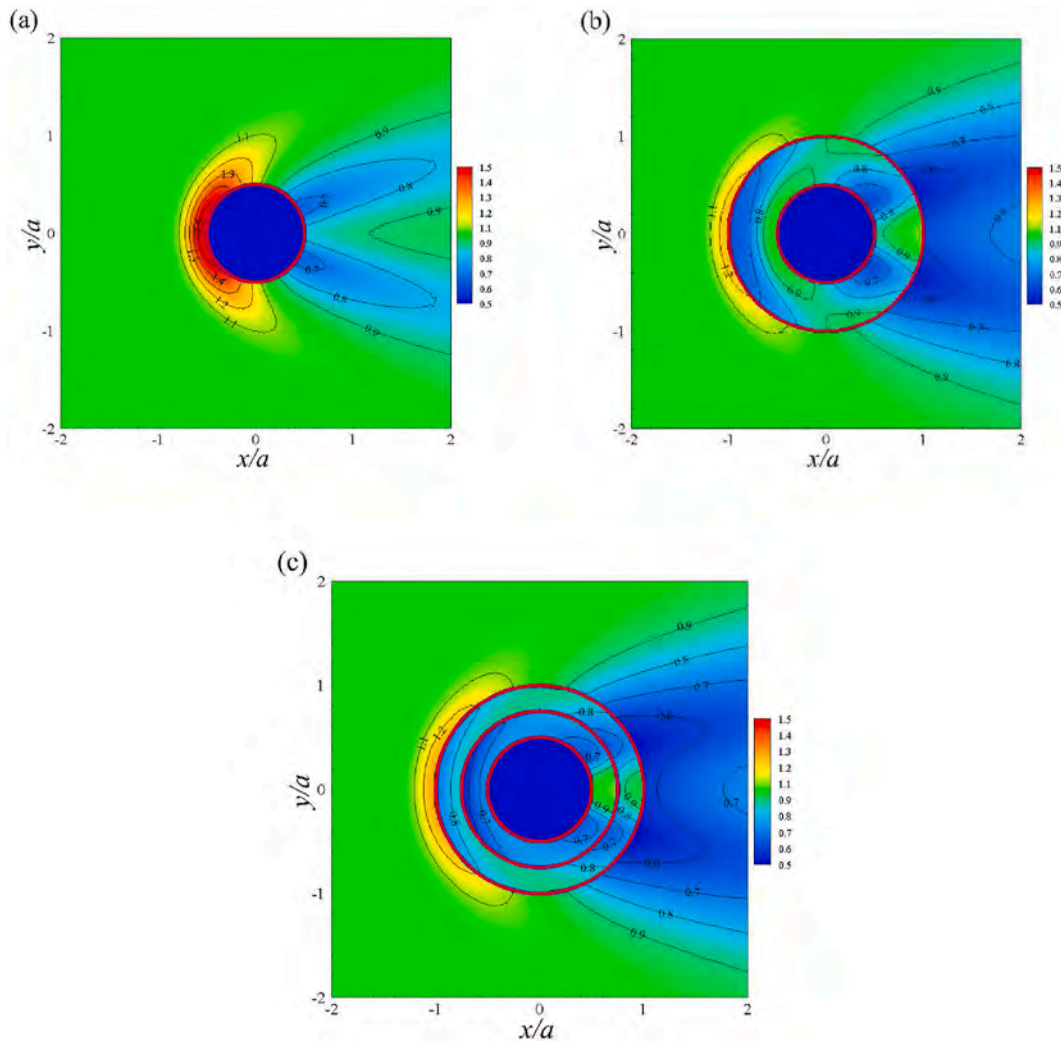
Fig. 16. The relative wave height in the vicinity of a concentric structure for different M: (a) $M = 0$, (b) $M = 1$, (c) $M = 2$.

4.5. Special case: solid cylinder with two concentric porous walls

The concentric three-cylinder system is a structure with high application potential (see, Fig. 10) and has been numerically studied by Liu et al. (2012) for short-crested interaction with a concentric cylindrical structure with double-layered perforated walls. Considering the potential value of the model for practical use in marine engineering, a separate discussion is necessary. In conjunction with the study of multi-layer structures, here, we select certain effective parameters to carry out the investigation of the hydrodynamic performance of concentric three-cylinder structures subjected to solitary waves. Here, the radius ratio of exterior wall to interior cylinder is set as $R_2/R = 2$, and the radius of the interior cylinder is $R = 10$m. For presentation convenience, a new variable of the distance ratio $\lambda = (R_1 - R)/(R_2 - R)$ is introduced.

It is important to study the effect of variation in the location of the middle porous wall on the dimensionless wave loads acting on the concentric structure. Fig. 11 demonstrates the wave forces$(F_2, F_1, F_{\text{int}})$ acting on the exterior wall, middle wall, and interior cylinder relative to the ratio $\lambda = (R_1 - R)/(R_2 - R)$ for various values of χ when $R_2/R = 2$, and $G_1 = G_2 = 1$. The exterior wall and interior cylinder experience decreasing wave loads as the middle wall gradually moves closer to the exterior wall from the interior cylinder, whereas the middle wall experiences increasing forces. In practical engineering, we are concerned with the forces on the interior cylinder, and the safety of the two porous walls. Therefore, it is likely to be an effective option when the middle

wall is positioned in the middle, i.e., $\lambda = 0.5$, wherein the wave load acting on the interior cylinder is near its minimum value and the middle wall is less expensive to construct. Moreover, the change of the location of the middle wall has the greatest effect on the wave force on the interior cylinder, which is related to the fact that the interior cylinder is a solid structure. Fig. 12 demonstrates the maximum dimensionless wave run-ups ($\eta_2, \eta_1, \eta_{\text{int}}$) acting on the concentric structure for different λ when $R_2/R = 2$, $G_1 = G_2 = 1$, and $\chi = 0.8$ With respect to the exterior wall and interior cylinder, the wave run-up in the leeward side decrease as λ increases, whereas a converse trend can be observed for the wave run-up in the leeward side of the middle wall. As indicated in Fig. 12c, λ has a higher influence on the wave run up on the leeward side than on the exterior or middle wall. This is similar to the results in Fig. 11.

Fig. 13 demonstrates the wave forces (F_2, F_1, F_{int}) acting on the exterior wall, middle wall, and interior cylinder relative to Gm ($G_1 = G_2$) for various values of χ when $R_2/R = 2$, and $\lambda = 0.5$. As shown in Fig. 13a and c, wave loads acting on the exterior wall are affected modestly by variations in χ, whereas the force on the interior cylinder is impacted significantly by χ. For a marginal G_m, the wave force acting on the middle wall increases gradually to a peak (Fig. 13b). Fig. 14 demonstrates the maximum dimensionless wave run-ups ($\eta_2, \eta_1, \eta_{\text{int}}$) acting on the three cylinders for different χ when $R_2/R = 2$, $G_1 = G_2 = 1$, and $\lambda = 0.5$. When $\theta/\pi < 0.4$, on the leeward side, the wave run-ups around the three structures decrease gradually as χ increases. It is noteworthy

that the minimum wave run-ups around the exterior wall, middle wall and interior cylinder occur at approximately $\theta/\pi = 0.18$, $\theta/\pi = 0.2$, and $\theta/\pi = 0.22$, i.e., a gradual left shift, which may be owing to the phase shift of the wave.

Fig. 15 shows the relative wave height variation near a concentric structure for varying $\lambda = (R_1 - R)/(R_2 - R)$ at $G_1 = G_2 = 1$, $R_2/R = 2$, and $\chi = 1.5$. It is evident that the variation in the location of the middle porous wall affected the surface elevation in the vicinity of the structure. Owing to the reflection effect of the middle wall, the surface elevation on the windward side of the exterior porous wall increased marginally when the middle porous wall was close to the exterior porous wall, whereas the surface elevation on the leeward side of the exterior porous wall decreased marginally. When the intermediate wall is approached the exterior wall, the concentric double porous walls provide better protection to the interior cylinder, i.e., the sheltering area increases. However, the sheltering area of the interior cylinder was not increased significantly when $\lambda > 0.4$, which implies that the radius of the middle wall does not need to be excessive.

Fig. 16 presents the relative wave height for three configurations at $\chi = 1.5$, $R_2/R = 2$, $G_1 = G_2 = 1$, and $\lambda = 0.5$. In Fig. 16a, the wave elevations at the free surface of a solid cylinder are determined, and these are relatively high. However, as shown in Fig. 16(b) and (c), concentric porous walls reduce the elevation near the impermeable cylinder surface. The concentric three-cylinder is significantly more complex than concentric two-cylinder structures in terms of elevations. On the windward side, the wave height is significantly lower near the interior cylinder than it would have been near one protected only by a porous wall, which owing to the secondary protection offered by the double walls. Meanwhile, on the leeward side, the wave height near the interior cylinder is marginally higher than it would have been near one protected only by a porous wall, which is because of the reflection effect of the middle wall. Overall, compared with the double-cylinder structure, the triple-cylinder structure is more reliable for protecting the interior cylinder against the more complex marine environment.

5. Conclusions

This paper presents an analytical investigation of solitary waves interaction with a concentric system having multiple porous outer walls. An analytical solution was obtained by using eigenfunction expression matching approach and separation-of-variable technique. The correctness of the analytical solution proposed in this paper is verified by comparing its values with the results of existing studies. The main conclusions obtained are as follows:

(1) The reduction in the amplitude of the wave force on the impermeable cylinder compared with that on an isolated cylinder ($M = 0$) is approximately 34%, 56%, 70%, 80%, and 87% for M of 1–5, respectively, which implies that sufficient protection can be achieved for the interior cylinder when $M = 2$ or 3. However, $M = 2$ may be the best option considering the construction cost.

(2) For multiple walls with different porous-effect parameters, the permutations of the selected porous-effect parameters have negligible effect on the wave force on the interior cylinder. However, the minimum wave run-up around it is observed when the coefficient of the porous walls increases from the outside to the inside. This indicate that porous walls wherein the coefficient of porosity decreases from the outside to the inside may be highly effective for concentric structures with multiple walls.

(3) A vertical impermeable cylinder with two concentric porous walls was also investigated considering its larger application prospects. The concentric three-cylinder is significantly more complex than concentric two-cylinder structures in terms of elevations. Owing to the secondary protection offered by the double walls, on the windward side, the wave height is significantly

smaller near the interior cylinder than it would be near one protected only by a porous wall.

Data availability

The data that support the findings of this study are available from the corresponding author upon reasonable request.

CRediT authorship contribution statement

Zhenfeng Zhai: Data curation, Writing – original draft, preparation, Visualization, Investigation, Software, Validation. **Weiwen Zhao:** Software, Data curation, Visualization, Investigation, Validation. **Decheng Wan:** Supervision, Conceptualization, Methodology, Investigation, Writing – review & editing. **Dan Liu:** help to revision.

Declaration of competing interest

The authors declare that they have no known competing financial interests or personal relationships that could have appeared to influence the work reported in this paper.

References

Basmat, A., 2002. Interaction of a solitary wave with a permeable cylindrical breakwater. In: PAMM: Proceedings in Applied Mathematics and Mechanics. Wiley Online Library, pp. 393–394.

Chwang, A., 1983. A porous-wavemaker theory. J. Fluid Mech. 132, 395–406.

Ghafari, A., Tavakoli, M.R., Nili-Ahmadabadi, M., Teimouri, K., Kim, K.C., 2021. Investigation of interaction between solitary wave and two submerged rectangular obstacles. Ocean. Eng. 237, 109659.

Hafsia, Z., Nouri, S., Boulaaras, S.M., Allahem, A., Alkhalaf, S., Vazquez, A.M., 2021. Solitary wave diffraction with a single and two vertical circular cylinders. Math. Probl Eng. 2021.

Isaacson, M.D.S.Q., 1983. Solitary wave diffraction around large cylinder. J. Waterw. Port, Coast. Ocean Eng. 109, 121–127.

Kuai, Y.r., Zhou, J.f., Duan, J.l., Wang, X., 2021. Numerical simulation of solitary wave forces on a vertical cylinder on a slope beach. China Ocean Eng. 35, 317–331.

Li, Y., Liu, Y., Teng, B., 2006. Porous effect parameter of thin permeable plates. Coast Eng. J. 48, 309–336.

Liang, H., Zheng, S., Shao, Y., Chua, K.H., Choo, Y.S., Greaves, D., 2021. Water wave scattering by impermeable and perforated plates. Phys. Fluids 33, 077111.

Liu, H., Zhang, L., Chen, H., Zhang, W., Liu, M., 2018. Wave diffraction by vertical cylinder with multiple concentric perforated walls. Ocean. Eng. 166, 242–252.

Liu, J., Lin, G., Li, J., 2012. Short-crested waves interaction with a concentric cylindrical structure with double-layered perforated walls. Ocean. Eng. 40, 76–90.

Mackay, E., Shi, W., Qiao, D., Gabl, R., Davey, T., Ning, D., Johanning, L., 2021. Numerical and experimental modelling of wave interaction with fixed and floating porous cylinders. Ocean. Eng. 242, 110118.

Miao, Y., Wang, K.H., 2019. Approximate analytical solutions for a solitary wave interacting with a partially submerged porous wall. Ocean. Eng. 181, 227–239.

Sankarbabu, K., Sannasiraj, S., Sundar, V., 2007. Interaction of regular waves with a group of dual porous circular cylinders. Appl. Ocean Res. 29, 180–190.

Sankarbabu, K., Sannasiraj, S.A., Sundar, V., 2008. Interaction of solitary waves with a group of dual porous circular cylinders. In: International Conference on Offshore Mechanics and Arctic Engineering, pp. 307–313.

Sarkar, A., Bora, S.N., 2021a. Exciting force for a coaxial configuration of a floating porous cylinder and a submerged bottom-mounted rigid cylinder in finite ocean depth. Arch. Appl. Mech. 1–19.

Sarkar, A., Bora, S.N., 2021b. Interaction of water waves with a semiporous bottom-mounted cylindrical storage tank containing a cylindrical pile. J. Waterw. Port, Coast. Ocean Eng. 147, 04021029.

Sollitt, C.K., Cross, R.H., 1973. Wave transmission through permeable breakwaters. Coast. Eng. 1827–1846.

Song, H., Tao, L.B., 2007. Short-crested wave interaction with a concentric porous cylindrical structure. Appl. Ocean Res. 29, 199–209.

Tao, L.B., Song, H., Chakrabarti, S., 2009. Wave interaction with a perforated circular breakwater of non-uniform porosity. J. Eng. Math. 65, 257–271.

Vijayalakshmi, K., Sundaravadivelu, R., Murali, K., Neelamani, S., 2008. Hydrodynamics of a concentric twin perforated circular cylinder system. J. Waterw. Port, Coast. Ocean Eng. 134, 166–177.

Wang, K.H., Ren, X., 1994. Wave interaction with a concentric porous cylinder system. Ocean. Eng. 21, 343–360.

Wang, P., Zhao, M., Du, X., Liu, J., 2019. Analytical solution for the short-crested wave diffraction by an elliptical cylinder. Eur. J. Mech. B Fluid 74, 399–409.

Wang, Q., Fang, Y., Liu, H., 2021. An experimental study of run-up and loads on a vertical truncated cylinder in a solitary wave. Ocean. Eng. 219, 108346.

Weng, Y., Xu, X., Huang, H., 2016. Interaction of cnoidal waves with an array of vertical concentric porous cylinders. Appl. Ocean Res. 58, 21–36.

Williams, A., Li, W., Wang, K.H., 2000. Water wave interaction with a floating porous cylinder. Ocean. Eng. 27, 1–28.

Yang, Z., Huang, B., Kang, A., Zhu, B., Han, J., Yin, R., Li, X., 2021. Experimental study on the solitary wave-current interaction and the combined forces on a vertical cylinder. Ocean. Eng. 236, 109569.

Zhai, Z., Shao, Y., Wang, K., Huang, H., Li, H., 2021. Semi-analytical solution of cnoidal wave diffraction around a double-layer arc-shaped vertical porous breakwater. J. Fluid Struct. 103, 103261.

Zhai, Z., Zheng, S., Wan, D., 2022. Interaction between solitary waves and a combined structure of two concentric asymmetric porous arc walls. Phys. Fluids 34, 042103.

Zheng, S., Meylan, M., Greaves, D., Iglesias, G., 2020. Water-wave interaction with submerged porous elastic disks. Phys. Fluids 32, 047106.

Zhu, D.T., 2011. Wave run-up on a coaxial perforated circular cylinder. China Ocean Eng. 25, 201–214.